

Efficient Brownian oscillators and nanoheaters based on Gallium-doped ϵ -Fe₂O₃

Yuanyu Gu^{a,b}, Nuno J.O. Silva,^c Marie Yoshikiyo,^d Asuka Namai,^d Rafael Piñol,^b Guillaume Maurin-Pasturel,^b
Yuwen Cui,^a Shin-ichi Ohkoshi^d and Angel Millán^b

- a. *School of Materials Science and Engineering, Nanjing Tech University, 210009, Nanjing PR China.*
- b. *Instituto de Ciencia de Materiales de Aragón, ICMA-CSIC/University of Zaragoza, C/ Pedro Cerbuna 10, 50006 Zaragoza (Spain).*
- c. *Departamento de Física and CICECO-Aveiro Institute of Materials, Universidade de Aveiro, 3810–193 Aveiro (Portugal).*
- d. *Department of Chemistry, School of Science, The University of Tokyo, 7-3-1 Hongo, Bunkyo-ku, Tokyo 113-0033, Japan.*

1. Magnetic hysteresis loops of $\epsilon\text{-Ga}_x\text{Fe}_{2-x}\text{O}_3$.

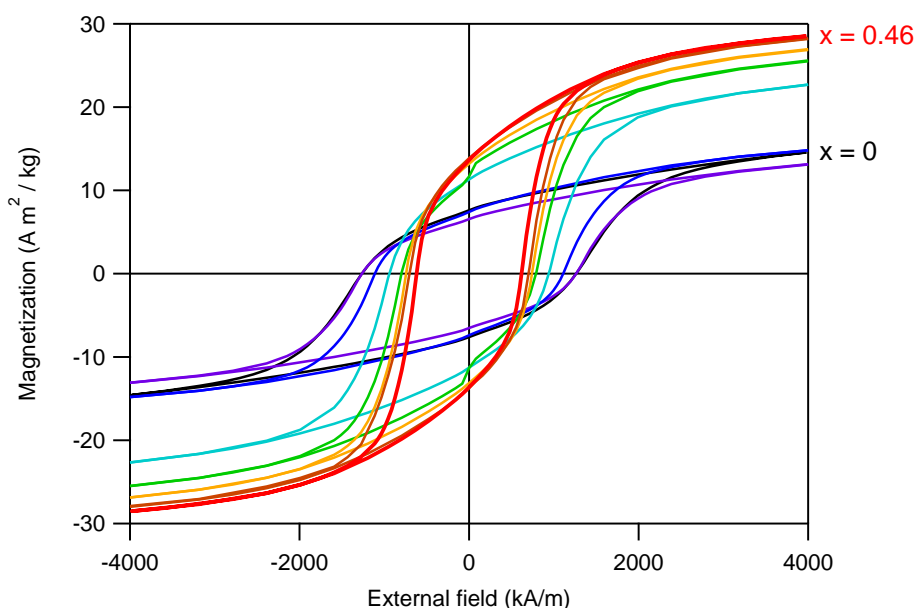


Fig. S11. Magnetic hysteresis loops of $\epsilon\text{-Ga}_x\text{Fe}_{2-x}\text{O}_3$ measured at 300 K for $x = 0$ (black),²⁰ 0.10 (purple),⁹ 0.15 (blue),⁹ 0.22 (light blue),⁹ 0.29 (green),⁹ 0.35 (orange),⁹ 0.40 (brown),⁹ and 0.46 (red). These magnetic hysteresis loops were measured with powder-form samples. The data were adapted from previous literatures,^{9,20} and the units were converted from CGS unit to SI unit [Adapted with permission from [ref. 9] *Angew. Chemie Int. Ed.*, 2007, 46, 8392–8395 ©2007 WILEY-VCH Verlag GmbH & Co. KGaA, Weinheim and [ref. 20] *RSC Adv.*, 2020, 10, 28786–28797 @ 2020 The Royal Society of Chemistry].

2. Structural information of $\epsilon\text{-Ga}_{0.46}\text{Fe}_{1.54}\text{O}_3$ by Rietveld analysis of the XRD pattern.

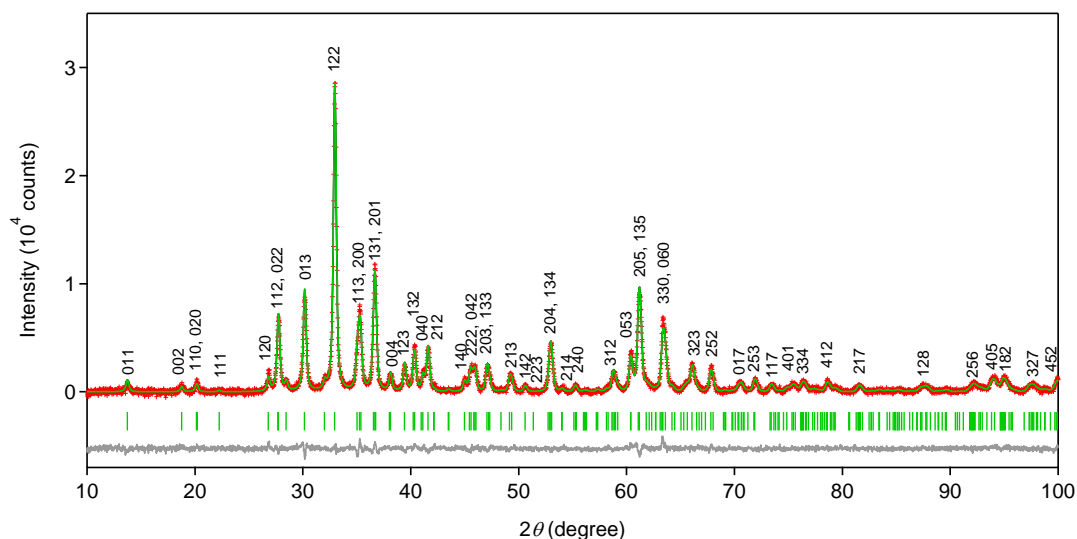


Fig. S12. XRD pattern, which shows that the NPs ($\text{Ga}_{0.46}\text{Fe}_{1.54}\text{O}_3$) are pure ϵ -phase. Red dots, green line, and grey line are the observed pattern, calculated pattern, and their difference, respectively. Green bars represent the calculated positions of the Bragg reflections of $\epsilon\text{-Ga}_{0.46}\text{Fe}_{1.54}\text{O}_3$. The crystalline size was estimated as 20 nm. The crystalline size from the Rietveld analysis is smaller than the observed particle size from the TEM image (25 nm) because there is a structure-disordered layer on the particle surface.

Table SI1. Structural parameters of $\epsilon\text{-Ga}_{0.46}\text{Fe}_{1.54}\text{O}_3$ obtained from Rietveld analysis of the XRD pattern. M stands for Fe or Ga.

Polymorph	$\epsilon\text{-Ga}_{0.46}\text{Fe}_{1.54}\text{O}_3$		
Crystal system	Orthorhombic		
Space group	$Pna2_1$ (No. 33)		
a (Å)	5.0881(3)		
b (Å)	8.7725(5)		
c (Å)	9.4365(4)		
V (Å ³)	421.21(4)		
Z	8		
R_{wp} (%)	0.92		
S	1.2041		
Atomic pos.	x/a	y/b	z/c
M(A)	0.319(2)	0.3502(15)	0.165(4)
M(B)	0.3191(12)	0.0316(4)	0.369(4)
M(C)	0.3114(9)	0.6568(7)	0.386(4)
M(D)	0.189(2)	0.8430(14)	0.080(5)
O(1)	0	0	0
O(2)	0.033(5)	0.325(2)	0.016(5)
O(3)	0.000(6)	0.657(3)	0.018(5)
O(4)	0.175(6)	0.490(2)	0.280(4)
O(5)	0.170(5)	0.844(3)	0.262(5)
O(6)	0.154(5)	0.163(3)	0.246(4)

3. Indexes of the SAED image.

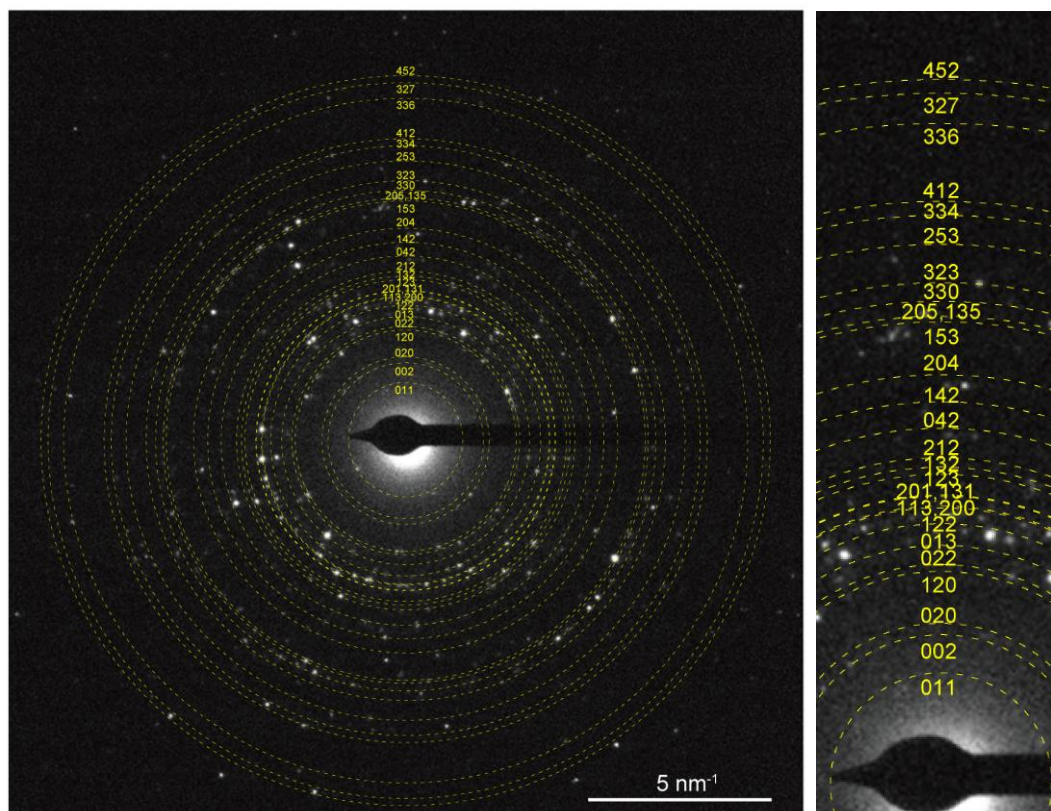


Fig. SI3. Electron diffraction pattern with indexes.

4. DLS intensity size distribution

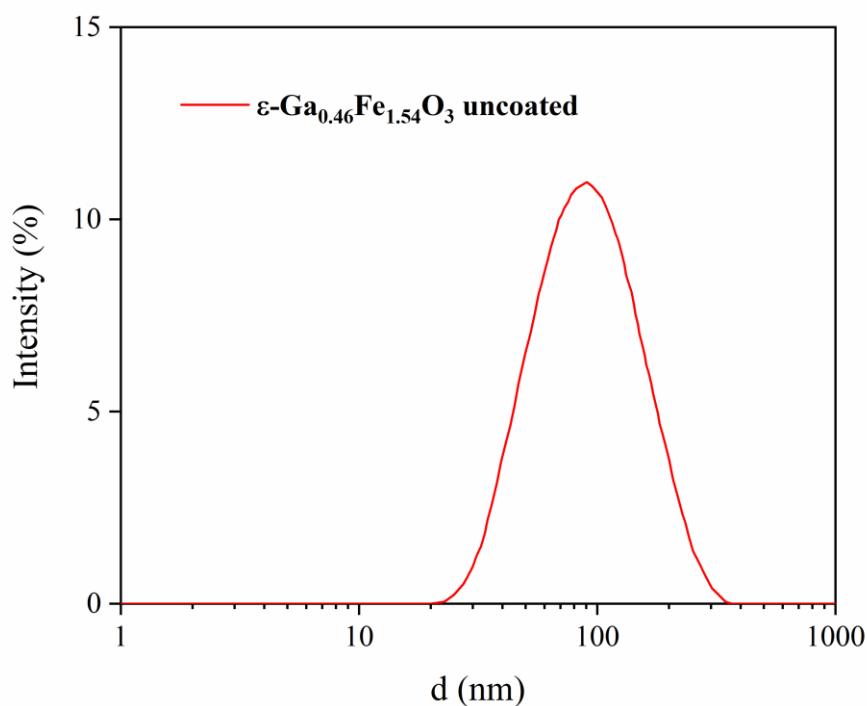


Fig S14. DLS intensity size distribution of uncoated of $\epsilon\text{-Ga}_{0.46}\text{Fe}_{1.54}\text{O}_3$ NPs.

The monomodal character of the DLS size distribution is an indication of a little presence of aggregations as an extensive aggregation would derive in a second population centred in a double, triple or higher average size value. This should be more noticeable in the DLS intensity size distribution, in which large nanoparticles are overrepresented due to their larger light dispersion. However, this distribution is monomodal (Fig S14) indicating a relative low presence of aggregates in the sample. A close inspection of TEM images did not reveal any crystalline grain boundaries from chemical aggregation, although the physical separation between the nanoparticles is occasionally small that is a consequence of evaporation of the suspension drops deposited on the grids during sample preparation. Moreover the crystal domain size obtained by applying Scherrer equation to XRD pattern yield values close to the TEM average particle size.

This size and hydrodynamic size distribution results in a distribution of dipolar energies, where, qualitatively, dipolar interactions may occur between nanoparticles with about the average size, between one nanoparticle high a size higher than average and another one lower, between nanoparticles with sizes lower than average, and between nanoparticles with sizes higher than average, the latter contributing to higher dipolar energies. In fact, we estimate that for $x=0$, two nanoparticles with a crystalline size of 50 nm will give a dipolar energy of the order of 1000 K. We also estimate that for $x=0.46$ (the sample with higher saturation magnetization and thus with higher dipolar energy), two nanoparticles with a crystalline size of 50 nm will give a dipolar energy of the order of 4000 K. This means that in a hypothetical sample with 50 nm NPs, thermal fluctuations would not dominate. Anyway, samples as those studied here with a small fraction of 50 nm are quite stable, and we speculate that this smaller fraction can be somehow equivalent to a lower concentration of these NPs, resulting in stability by larger interparticle distances.

5. Heating curves and SAR calculations

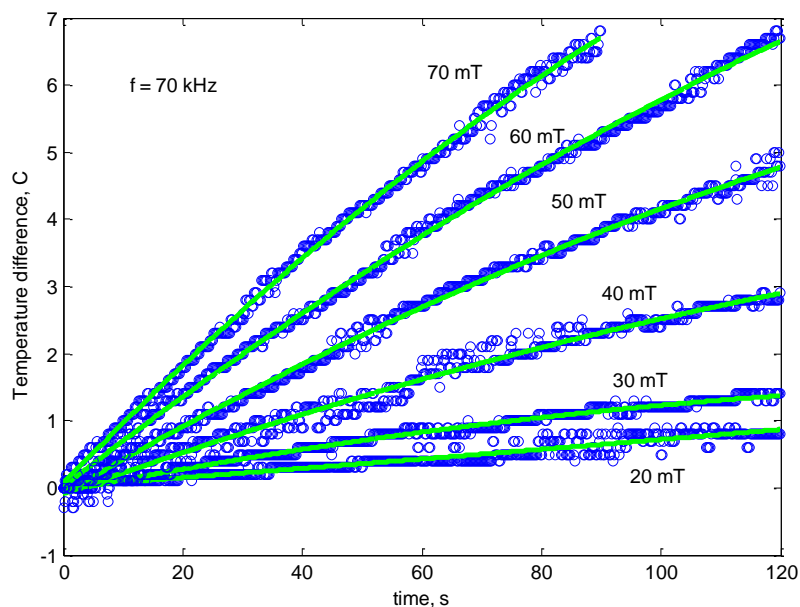


Fig. S15. Heating curves (abscissa axis is the time, and the vertical axis is the temperature difference between the sample and the water reference) of $\epsilon\text{-Ga}_{0.46}\text{Fe}_{1.54}\text{O}_3$ NPs in aqueous suspension (3.3 mg/ml) under different magnetic fields. The points are experimental measurements, and the green lines are the fittings to second order of polynomial.

The SAR values were extracted from the $T(t)$ curves, by using the equation below:

$$SAR = \frac{C_{\text{H}_2\text{O}}}{c_{\text{GaFeO}}} \frac{\Delta T}{\Delta t}$$

with $C_{\text{H}_2\text{O}}$ the heat capacity of water, c_{GaFeO} the concentration of $\epsilon\text{-Ga}_{0.46}\text{Fe}_{1.54}\text{O}_3$ NPs, and $\Delta T/\Delta t$ the initial slop of the heating curves (Fig. S15), which was calculated from the derivative of a polynomial obtained by fitting experimental data to a second order polynomial.

6. SAR values of pure epsilon- Fe_2O_3 NPs in water suspension.

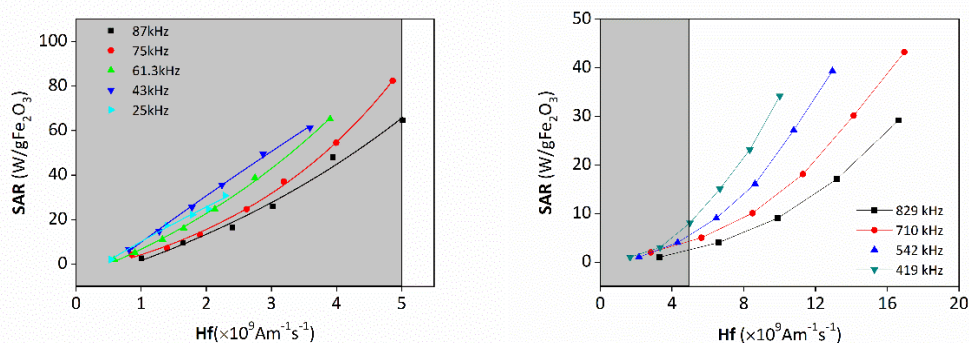


Fig. S16. SAR vs Hf plots of pure $\epsilon\text{-Fe}_2\text{O}_3$ NPs in water suspension at both low and high frequencies. For instance, a SAR value of 100 W/g means that one gram of NPs in solution deliver a total heat of 200 J per second of application of the field ac magnetic field.

7. SAR values of $\epsilon\text{-Ga}_{0.46}\text{Fe}_{1.54}\text{O}_3$ NPs in water suspension at high frequencies.

As shown in Figure S17, when using magnetic field with high frequencies (419 to 829 kHz), SAR vs H curves have an exponential or second order polynomial shape, where no big difference of the SAR among the four frequencies can be noticed. However, the SAR vs Hf curves are noticeably separated with respect to the frequencies, indicating that $\epsilon\text{-Ga}_{0.46}\text{Fe}_{1.54}\text{O}_3$ NPs heat more effectively when decreasing the frequency from 829 to 419 kHz. The biggest SAR value reached in the high frequency range is 68.3 W/g at 710 kHz with magnetic field 23.9 kAm^{-1} , which is about one third compared with the biggest SAR value obtained in the low frequency range, and when considering the safety limit, the SAR values (below 14 W/g) at the four high frequencies are almost negligible.

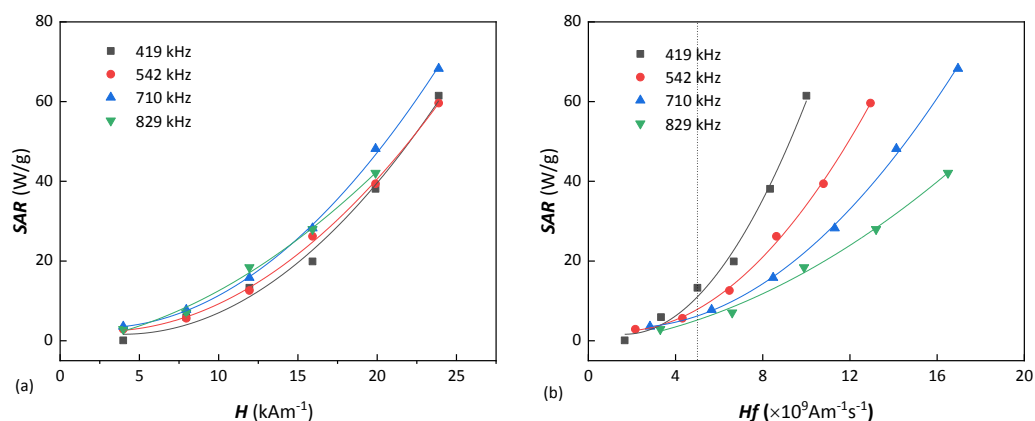


Fig. S17. SAR values at high frequencies of $\epsilon\text{-Ga}_{0.46}\text{Fe}_{1.54}\text{O}_3$ NPs in aqueous suspension as a function of magnetic field amplitude H (a) and Hf (b), respectively, in which the safety limit is marked as a dotted line. Solid lines are guides for the eyes.

8. Estimation of anisotropy energy.

The anisotropy energy of $\epsilon\text{-Ga}_{0.46}\text{Fe}_{1.54}\text{O}_3$ and $\epsilon\text{-Fe}_2\text{O}_3$ NPs at 300 K was estimated from the measured saturation magnetization M_S and coercivity H_C by using the equation, $H_C = \frac{2K}{\mu_0 M_S}$. Ref(1,2)

Table S12. Estimation of anisotropy energy K for both $\epsilon\text{-Ga}_{0.46}\text{Fe}_{1.54}\text{O}_3$ and $\epsilon\text{-Fe}_2\text{O}_3$ NPs at 300 K

sample	M_S (Am^{-1})	H_C (Am^{-1})	K (J/m^3)
$\epsilon\text{-Ga}_{0.46}\text{Fe}_{1.54}\text{O}_3$	149625	621000	58400
$\epsilon\text{-Fe}_2\text{O}_3$	68250	1592000	68300

This anisotropy is essentially magnetocrystalline (Ref. 1), and although some nanoparticles are elongated the contribution to anisotropy due to shape is expected (Ref. 3) to be an order of magnitude lower:

$$K_{shape} = 1/4\mu_0 M_S^2 (1 - 3N)$$

with $N \sim 0.2$, $K_{shape} \sim 2 \times 10^3 \text{ J/m}^3$

9. Calculation of relaxation times.

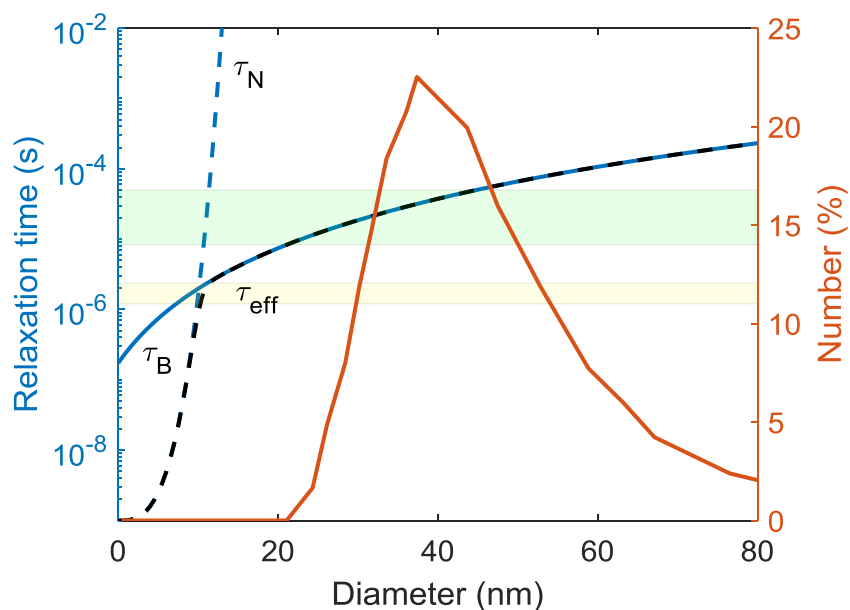


Fig. S18. Calculated relaxation times versus diameter of $\epsilon\text{-Ga}_{0.46}\text{Fe}_{1.54}\text{O}_3$ NPs in **aqueous** suspension at 300 K, including Néel (blue dashed line), Brownian (blue solid line), and the effective (black dashed line) relaxation times. The orange solid line represents the hydrodynamic size distribution from DLS measurement, and the green and yellow shadows correspond to the low frequency range (from 20 kHz to 120 kHz) and high frequency range (from 419 kHz and 829 kHz) used in the hyperthermia experiment, respectively. Estimations considered NPs with a 4 nm thick layer according to the TEM and DLS sizes, and the anisotropy energy given in **Table S12**.

The Néel relaxation time is proportional to the exponential of the product magnetocrystalline anisotropy and volume of the nanoparticles, while the Brownian relaxation time is proportional to the product of viscosity and volume of the nanoparticles being the effective mechanism for nanoparticles above ~ 12 nm and determining its behavior on ac susceptibility and hyperthermia experiments. The TEM and DLS sizes are close enough such that we conclude that the nanoparticles are isolated in the colloidal dispersions and therefore the relaxation times are dominated by single-particle properties.

In this graph, a τ_B value smaller than τ_N means that a NP with that size in water will respond to the external field with a physical rotation. In addition, the NPs with a size corresponding to a τ_B that “matches” the external field period used in the hyperthermia experiments will contribute to heat dissipation.

10. SAR values of other types of magnetic NPs proposed for hyperthermia therapy

Iron (III) oxide is by far the preferred type of NP for magnetic hyperthermia because of their biocompatibility, chemical stability and easy functionalization.⁴ Therefore, in order to establish the relative performance of Ga-doped $\epsilon\text{-Fe}_2\text{O}_3$ NPs presented here it is interesting to compare it with $\gamma\text{-Fe}_2\text{O}_3$ NPs of a similar size. Moreover, reviews about comparative SAR values of magnetic nanoparticles proposed for magnetic hyperthermia therapy can be found in references [4-7]. Table S13 presents SAR values of iron oxide NPs that are commercially available, extracted from ref. [5]. These values are clearly lower than that of our sample at similar Hf field conditions. Table S14 shows SAR values from other proposed NPs for magnetic hyperthermia. Some of the SAR values are larger than in our case but they correspond mostly to toxic substances or to field conditions outside the safety limits. Reported SAR values for magnetosomes present a large variation depending on the author.

Table S13. SAR reported values of some commercial iron oxide nanoparticle formulations in comparison with those of Ga-doped ϵ -Fe₂O₃, pure ϵ -Fe₂O₃ and γ -Fe₂O₃. The value in shaded file is outside the health safety limit.⁸

Samples	Size (nm)	Ms Am ² /kg	f (kHz)	H (kA/m)	H•f (x10 ⁻⁹ kA/m.s)	SAR (W/g*)	Ref.
ϵ -Ga _x Fe _{2-x} O ₃	25	28	60	83	5,E+09	286	this paper
ϵ -Fe ₂ O ₃	20	10	75	66	5,E+09	114	[9]
γ -Fe ₂ O ₃	20	74	90	55	5,E+09	229	[9]
NanoTherm			100	7	7,E+08	10	[10]
Resovist	10.5		900	5,7	5,E+09	63	[11]
FluidMag-D	12.7		900	5,7	5,E+09	56	[11]
FluidMag-CT			950	12	1,E+10	94	[6]
Nanomag-D-spio	11.2		900	5,7	5,E+09	63	[11]

*Notice that the SAR is given here per gram of metal

Table S14. SAR of NP compounds proposed for magnetic hyperthermia extracted from ref [5]. Values obtained at fields exceeding the safety conditions are shaded in light grey, and files in dark grey correspond to substances containing toxic ions such as Co.

Samples	Size (nm)	Ms Am ² /kg	f (kHz)	H (kA/m)	H•f (x10 ⁻⁹ kA/m.s)	SAR (W/g*)	Ref.
Mg _{0.13} @ γ -Fe ₂ O ₃	7		110	11,14	1,E+09	191	[12]
Fe _{0.6} Mn _{0.4} O ₄	102,7	6	366	32	1,E+10	535	[13]
Zn _{0.4} Mn _{0.6} Fe ₂ O ₄	15	175	500	3,7	2,E+09	432	[14]
Fe ₃ O ₄	22	65	500	15,5	8,E+09	716	[15]
MnFe ₂ O ₄ @CoFe ₂ O ₄	15	100	500	37,3	2,E+10	3034	[16]
CoFe ₂ O ₄ @Ni _{0.5} Zn _{0.5} Fe ₂ O ₄	9	28,2	265	30	8,E+09	25	[17]
Fe@Fe ₃ O ₄	13	164	170	26,4	4,E+09	140	[18]
FePt@Fe ₃ O ₄	15	36	630	18,8	1,E+10	1120	[19]
Magnetosomes	30	-	410	10	4,E+09	960	[20]
Magnetosomes	40		198	15,2	3,E+09	40	[21]
Magnetosomes	35	61,4	750	5	4,E+09	171	[22]
Magnetosomes	45		75	30	2,E+09	375	[23]
Zn _{0.4} Fe _{2.6} O ₄	18	165	500	37,4	2,E+10	1860	[24]
CoFe ₂ O ₄ @Zn _{0.4} Fe _{2.6} O ₄	60	190	500	37,4	2,E+10	10600	[16]

Notice that the SAR is given here per gram of metal

11. Instruments.

Elemental analysis was performed by X-ray fluorescence (XRF) using Rigaku ZSX Primus II. The ratio of Fe:Ga was 77.2:22.8, indicating the sample formula of $x = 0.46$.

X-ray diffraction (XRD) measurement was performed using Rigaku Ultima IV with Cu K α radiation ($\lambda = 1.5418 \text{ \AA}$). Rietveld analysis for the XRD pattern was performed using Rigaku PDXL software. TEM observations were conducted on a FEI Tecnai TF20 microscope with carbon coated copper grids after dip coating of the grids in the

ferrofluid samples. Dynamic light scattering (DLS) measurements were performed on Zetasizer Nano ZS from Malvern Laser. Magnetic measurements of samples were carried out on a SQUID-Based Magnetometer MPMS-XL5 from Quantum Design.

References

- 1 J. Jin, S. Ohkoshi and K. Hashimoto, *Adv. Mater.*, 2004, 16, 48-51.
- 2 A. H. Morrish, *The physical principles of magnetism*, 2001.
- 3 Coey, J. (2010). *Magnetism and Magnetic Materials*. Cambridge: Cambridge University Press. doi:10.1017/CBO9780511845000.
- 4 D. Chang, M. Lim, J. A. C. M. Goos, R. Qiao, Y. Ye. Ng, F. M. Mansfeld, M. Jackson, T. P. Davis and M. Kavallaris, *Front. Pharmacol.* 2018, 9, 831.
- 5 X. Liu, Y. Zhang, Y. Wang, W. Zhu, G. Li, X. Ma, Y. Zhang, S. Chen, S. Tiwari, K. Shi, S. Zhang, H. M. Fan, Y. X. Zhao and X. J. Liang, *Theranostics* 2020, 10, 3793-3815.
- 6 C. Blanco-Andujar, D. Ortega, P. Southern, Q. A. Pankhurst and N. T. K. Thanh, *Nanoscale*, 2015, 7, 1768-1775.
- 7 C. Blanco-Andujar, F. J. Teran and D. Ortega in: *Iron Oxide Nanoparticles for Biomedical Applications*, M. Mahmoudi and S. Laurent eds. Elsevier 2018, pags. 197-245.
- 8 R. Hergt and S. Dutz, *J. Magn. Magn. Mater.* 2007, 311, 187-192.
- 9 Y. Gu, M. Yoshikiyo, A. Namai, D. Bonvin, A. Martinez, R. Piñol, P. Téllez, N. J. O. Silva, F. Ahrentorp, C. Johansson, J. Marco-Brualla, R. Moreno-Loshuertos, P. Fernández-Silva, Y. Cui, S. Ohkoshi and A. Millán, *RSC Adv.*, 2020, 10, 28786-28797.
- 10 K. Maier-Hauff, F. Ulrich, D. Nestler, H. Niehoff, P. Wust, B. Thiesen, H. Orawa, V. Budach and A. Jordan, *J. Neurooncol.* 2011, 103, 317-324.
- 11 M. Kallumadil, M. Tada, T. Nakagawa, M. Abe, P. Southern and Q. A. Pankhurst, *J. Magn. Magn. Mater.* 2009, 321, 3650-3651.
- 12 X. Liu, M. Peng, G. Li, Y. Miao, H. Luo and G. Jing, et al. *Nano Lett.* 2019, 19, 4118-25.
- 14 X. L. Liu, C. T. Ng, P. Chandrasekharan, H. T. Yang, L. Y. Zhao, E. Peng, et al. *Adv. Health Mater.* 2016, 5, 2092-104.
- 15 R. Chen, M. G. Christiansen, P. Anikeeva, *ACS Nano* 2013, 7, 8990-9000.
- 16 J. H. Lee, J. T. Jang, J. S. Choi, S. H. Moon, S. H. Noh, J. W. Kim, et al. *Nat Nanotechnol* 2011, 6, 418-22.
- 17 M. R. Phadatare, J. V. Meshram, K. V. Gurav, J. H. Kim, S. H. Pawar *J. Phys. D Appl. Phys.* 2016, 49, 95004.
- 18 L. M. Lacroix, N. Frey Huls, D. Ho, X. Sun, K. Cheng and Sun S. *Stable Lett.* 2011, 11, 1641-5.
- 19 M. D. Yang, C. H. Ho, S. Ruta, R. Chantrell, K. Krycka, O. Hovorka, et al. *Adv Mater.* 2018, 30, 1802444.
- 20 R. Hergt, R. Hiergeist, M. Zeisberger, D. Schuler, U. Heyen, I. Hilger, et al. *J Magn Magn Mater.* 2005, 293, 80-6.
- 21 R. Le Fevre, M. Durand-Dubief, I. Chebbi, C. Mandawala, F. Lagroix, J. P. Valet, et al. *Theranostics* 2017, 7, 4618-31.
- 22 M. Timko, A. Dzarova, J. Kovac, A. Skumiel, A. Jozefczak, T. Hornowski, et al. *J. Magn. Magn. Mater.* 2009, 321, 1521-4.
- 23 A. Muela, D. Muñoz, R. Martín-Rodríguez, I. Orue, E. Garaio, A. Abad Díaz de Cerio, et al. *J. Phys. Chem. C* 2016, 120, 24437-48.
- 24 S. H. Noh, W. Na, J. T. Jang, L. H. Lee, E. J. Lee, S. H. Moon, et al. *Nano Lett.* 2012, 12:, 3716-21.